Quantitative measurements and modeling of cargo–motor interactions during fast transport in the living axon

Pamela E Seamster[1,6]**, Michael Loewenberg**[1,2,3,6]**, Jennifer Pascal**[1]**, Arnaud Chauviere**[1,5]**, Aaron Gonzales**[1]**, Vittorio Cristini**[1,2] **and Elaine L Bearer**[1,4,7]

[1] Department of Pathology, University of New Mexico Health Sciences Center, Albuquerque, NM 87131, USA
[2] Department of Chemical and Nuclear Engineering, University of New Mexico, Albuquerque, NM 87131, USA
[3] Department of Chemical and Environmental Engineering, Yale University, New Haven, CT 06520, USA
[4] Marine Biological Laboratory, an affiliate of Brown University, Woods Hole, MA 02543, USA

E-mail: Elaine.Bearer@gmail.com

Abstract

The kinesins have long been known to drive microtubule-based transport of sub-cellular components, yet the mechanisms of their attachment to cargo remain a mystery. Several different cargo-receptors have been proposed based on their *in vitro* binding affinities to kinesin-1. Only two of these—phosphatidyl inositol, a negatively charged lipid, and the carboxyl terminus of the amyloid precursor protein (APP-C), a trans-membrane protein—have been reported to mediate motility in living systems. A major question is how these many different cargo, receptors and motors interact to produce the complex choreography of vesicular transport within living cells. Here we describe an experimental assay that identifies cargo–motor receptors by their ability to recruit active motors and drive transport of exogenous cargo towards the synapse in living axons. Cargo is engineered by derivatizing the surface of polystyrene fluorescent nanospheres (100 nm diameter) with charged residues or with synthetic peptides derived from candidate motor receptor proteins, all designed to display a terminal COOH group. After injection into the squid giant axon, particle movements are imaged by laser-scanning confocal time-lapse microscopy. In this report we compare the motility of negatively charged beads with APP-C beads in the presence of glycine-conjugated non-motile beads using new strategies to measure bead movements. The ensuing quantitative analysis of time-lapse digital sequences reveals detailed information about bead movements: instantaneous and maximum velocities, run lengths, pause frequencies and pause durations. These measurements provide parameters for a mathematical model that predicts the spatiotemporal evolution of distribution of the two different types of bead cargo in the axon. The results reveal that negatively charged beads differ from APP-C beads in velocity and dispersion, and predict that at long time points APP-C will achieve greater progress towards the presynaptic terminal. The significance of this data and accompanying model pertains to the

---

[5] New Mexico Center for the Spatiotemporal Modeling of Cell Signaling.
[6] These authors contributed equally.
[7] Author to whom any correspondence should be addressed.

role transport plays in neuronal function, connectivity, and survival, and has implications in the pathogenesis of neurological disorders, such as Alzheimer's, Huntington and Parkinson's diseases.

S Online supplementary data available from stacks.iop.org/PhysBio/9/055005/mmedia

Introduction

The internal environment of the eukaryotic cell is a beehive of constantly moving parts. Subcellular particles move rapidly to and fro at amazing velocities of up to 5 μm s^{-1}, as first revealed by video-enhanced differential-interference-contrast (DIC) microscopy of cells (Allen *et al* 1981, 1982b) and also witnessed inside the dissected giant axon of the squid (Allen *et al* 1982a). After extrusion from the axon sheath, axoplasm sustains such motility (Brady *et al* 1982), which ultimately allowed the tracks, microtubules (Schnapp *et al* 1985), and motor, kinesin, to be discovered (Vale *et al* 1985a). Much excitement focused on the kinesin motor domain and its ability to harvest chemical energy from ATP hydrolysis to produce force and walk along the microtubule. The other end of the motor, its cargo-binding domain, has received less attention and far less progress has been made in defining how it binds to transport vesicles. A major obstacle has been the large amount of soluble kinesin-1 in cytoplasm and its ability to bind and transport negatively charged beads (Vale *et al* 1985b). This physiologically effective yet apparently non-specific promiscuity has complicated the discovery of specific molecular interactions mediating binding of motors to particular cargo.

The squid giant axon continues to be a powerful physiological tool for discovery of transport mechanics (Kanaan *et al* 2011, Morfini *et al* 2009, Satpute-Krishnan *et al* 2006, Solowska *et al* 2008, Terada *et al* 2010). The giant axon continues to display active transport for up to 6 h after dissection. Its translucency allows imaging of such transport within the deeper microtubule-rich axoplasm. Its large size, up to 1 mm in diameter and 7 cm in length, facilitates injection of large molecules, engineered cargo and inhibitors (Bearer *et al* 2000, Galbraith *et al* 1999, Satpute-Krishnan *et al* 2003, Terasaki *et al* 1995). There is no other system that provides the combined ability to control the precise surface properties of cargo and witness cargo behavior in a living intact axon.

We engineer cargo and then test for relative ability to transport in this powerful squid axon model (Bearer *et al* 2000, Satpute-Krishnan *et al* 2003, 2006). Initially we used the human herpes simplex virus type 1 (HSV1) as cargo. This virus secondarily enters sensory nerve endings in infected mucus membranes and then travels retrograde within the neuronal process to reach its cell body, where the viral DNA is released into the nucleus to enter latency or to replicate. Upon replication, nascent viral particles are packaged in the perinuclear region and then travel anterograde within the sensory nerve process to emerge at the mucus membrane, thereby causing the recurrent 'cold sore'. Hence we reasoned that HSV1 'knew' how to direct its transport in either the anterograde or retrograde direction, a necessary part of regulating its life cycle. By labeling virus during its synthesis in cell culture with green fluorescent protein (GFP), isolating viral particles and stripping them of viral envelope and cellular membranes with detergent, we biochemically engineered the HSV viral particle to display only the inner tegument proteins and to be detectible by fluorescence laser-scanning confocal microscopy in the axon. After injection into the squid giant axon, such engineered viral particles transported uniquely in the retrograde direction (Bearer *et al* 2000). When not stripped of membrane, GFP-labeled viral particles transported anterograde (Satpute-Krishnan *et al* 2003). We thus proposed that the viral receptor for the anterograde motor machinery must reside in the stripped membrane whose absence eliminated anterograde and revealed retrograde capability. Analysis of the proteins in the membrane extract demonstrated a high abundance of amyloid precursor protein (APP) (Satpute-Krishnan *et al* 2003), a kinesin-binding protein (Kamal *et al* 2000) thought to mediate vesicular transport (Kamal *et al* 2001, Reis *et al* 2012, Szpankowski *et al* 2012). APP is also known to be the parent protein that produces Abeta, a major component of pathognomonic senile plaques found in brains of Alzheimer's disease.

By creating another type of engineered cargo, peptide-conjugated fluorescent nanospheres, we were able to test directly for transport capacity of the cytoplasmic domain of APP (Satpute-Krishnan *et al* 2006). When conjugated to 100 nm nanospheres a 15-amino acid domain at the carboxyl terminus of the cytoplasmic tail of APP was sufficient to render beads motile in the anterograde direction in the squid giant axon. In contrast peptides derived from the extracellular domain of APP or synthesized with the same amino acid content in a different order, were not motile (Satpute-Krishnan *et al* 2006). This first report demonstrated a new assay for cargo signatures involved in recruitment of transport machinery and its successful application to one such signature, carboxyl terminus of APP (APP-C). However, the assay was limited without control beads for either non-motile or motile activities to serve as internal monitors for non-specific movements due to axoplasmic flow or for lack of movement due to loss of axonal transport activity. Here we report the development and characterization of these two valuable control beads: glycine-conjugated COOH beads that display the carboxyl group of the glycine but are not motile, and washed COOH (negatively charged) beads, that are actively motile via non-peptide specific interactions with transport machinery, as had previously been shown *in vitro* (Terasaki *et al* 1995, Vale *et al* 1985b). By comparing the activity of each of these control beads with the known cargo-receptor previously reported by us, APP-C, we definitively show their value as controls, and

demonstrate that the peptide cargo receptor, APP-C, is more effective than negative charge to mediate transport.

These experiments using defined cargo are unique. Such precise control of the surface of cargo cannot be obtained by driving expression of putative motor receptors inside cells, since hundreds of other molecules are typically displayed on the cytoplasmic surface of endogenous organelles. Since the beads are fluorescent and large enough to image in the axon by confocal laser scanning microscopy, we obtain significant biophysical information about the movements of such single-species beads at the micron and second scales within the living axon. Qualitative observations can be used to develop mathematical models. Subsequently more precise biophysical measurements of bead behavior can be compared with the output of these models predicting cargo–motor interactions. Particularly useful parameters for informing mathematical models are pause frequency and duration, run lengths and durations, and velocities.

Recently, models of slow transport based on both fluorescence microscopy of labeled proteins and on radioactive tracer measurements have revealed new insights on slow transport of neurofilaments inside living axons (Brown *et al* 2005, Jung and Brown 2009, Li *et al* 2012). Beeg *et al* compared experimental and theoretical results for multi-motor cargo transport in a traditional *in vitro* system, using purified kinesin-1 passively adsorbed to carboxylated polystyrene beads, and imaging movements on purified microtubules with conventional DIC widefield microscopy. They also generated interesting models for transport in this simplified recombination system (Beeg *et al* 2008). Here, we employ the traffic model proposed by Smith and Simmons (2001) to describe the dynamics of transport of mobile and immobile cargo within the living axon and compare the calculated model predictions for the cumulative spatio-temporal distributions of cargo to the results from our experimental data.

Below we present our new experiments with carboxylated and de-activated controls, explain our methodology for quantifying cargo transport mediated by specific receptors, the results of our biophysical measurements, and further show companion biochemical analysis of the motors involved. We then describe the mathematical approach that we employ to predict the dynamics of these complex multifactorial interactions within the axon that result in selective cargo movements. We validate the mathematical model through comparison with detailed statistical analyses of bead transport data from living axons. Finally we show that APP-C-conjugated cargo achieves greater distance towards the synapse than negatively charged cargo.

Experimental procedures

Cargo engineering

Carboxylated microspheres (beads, 100 nm diameter) red fluorescent (580/605 nm; Molecular Probes/Invitrogen, Grand Island, NY) or green fluorescent (Dragon Green, 505/515 nm; Bangs Laboratories, Inc., Fishers IN) are washed by a Microcon-30 kDa Centrifugal Filter Unit with Ultracel-30

membrane with 100 nm cut-off (Millipore). Briefly, 125 μL of a 2% suspension of beads is mixed with 125 μL of ddH$_2$0 in the Microcon filter tube and spun for 6 min at 13 000 $\times$ g in an Eppendorf microfuge. The fluid is removed and the beads in the upper chamber resuspended in 125 μL ddH$_2$0 three more times to dilute out the concentration of azide in the storage buffer. The microcon filter is then inverted and spun at 1000 $\times$ g for 3 min to remove the beads from the tube. For injection of un-conjugated negatively charged beads, the washed beads are resuspended in $\frac{1}{2}$ X, a buffer consistent with internal axoplasmic conditions (Brady *et al* 1982). For conjugations, beads are resuspended in ddH$_2$0 to a total volume of 125 μL to maintain 2% solid/volume ratio of the original suspension.

Candidate peptides were synthesized based on amino acid sequences from the NCBI GenBank database (Aves Labs, Inc., Tigard, OR) and covalently cross-linked by their amino terminus to the carboxylic acid moiety on the beads (figure 1) according to a modification of method in Satpute-Krishnan *et al* (2006). Relevant to this report, our diagram shows the orientation of the carboxylic acid residue on the bead conjugates. Negative charge has long been known to attract kinesin-1. Because of this relatively non-specific charge-based interaction, motors are likely to passively adsorb to these beads.

Briefly 10 μL of the washed bead suspension are first activated by incubation in 500 μL of 100 mM MES buffer pH 6.0 with 5 μL of 1-Ethyl-3-(3-dimethylaminopropyl)carbodiimide hydrochloride (EDC, Thermo Scientific, Rockford, IL) from 200 mM solution (EDC final concentration, 2 mM) and 25 μL of *N*-hydroxysulfosuccinimide (Sulfo-NHS, Thermo Scientific) from 100 mM solution (Sulfo-NHS final concentration, 5 mM) and incubated for 15 min on a rotating navigator. Then, 20 μL of peptide solution (0.25 to 2.0 mg mL^{-1} stock in ddH$_2$0), 1.4 μL β-mercaptoethanol (BME; final concentration, 20 mM is added) and the pH adjusted to 7.5 with 2–3 μL of 10 N NaOH, as tested with pH indicator paper. After 2 h at room temperature on the rotator, the reaction is quenched by adding 2M glycine (Sigma) to a final concentration of 0.1 M or with 20 mM ethanolamine and incubated another 30 min on the rotator. As controls beads are processed in parallel but without peptide such that the final quenching step adds glycine or ethanolamine to the activated moieties on the surface; or a non-motility peptide is added, such as one derived from the amino, luminal, domain of APP or a peptide with the same amino acid composition as the C-terminal but in a different order (jumbled).

Conjugated beads are washed free of chemicals by microfuging in the microcon filter three times, and resuspended in 250 μL of ddH$_2$0. Conjugated beads may be stored for several days at 4 $^\circ$C. When clumping occurs, they can no longer be used.

Squid axonal dissection and injections

Giant axons were dissected from North Atlantic Long-Finned Squid (*Loligo pealleii*) in Ca^{2+}-free sea water at the Marine
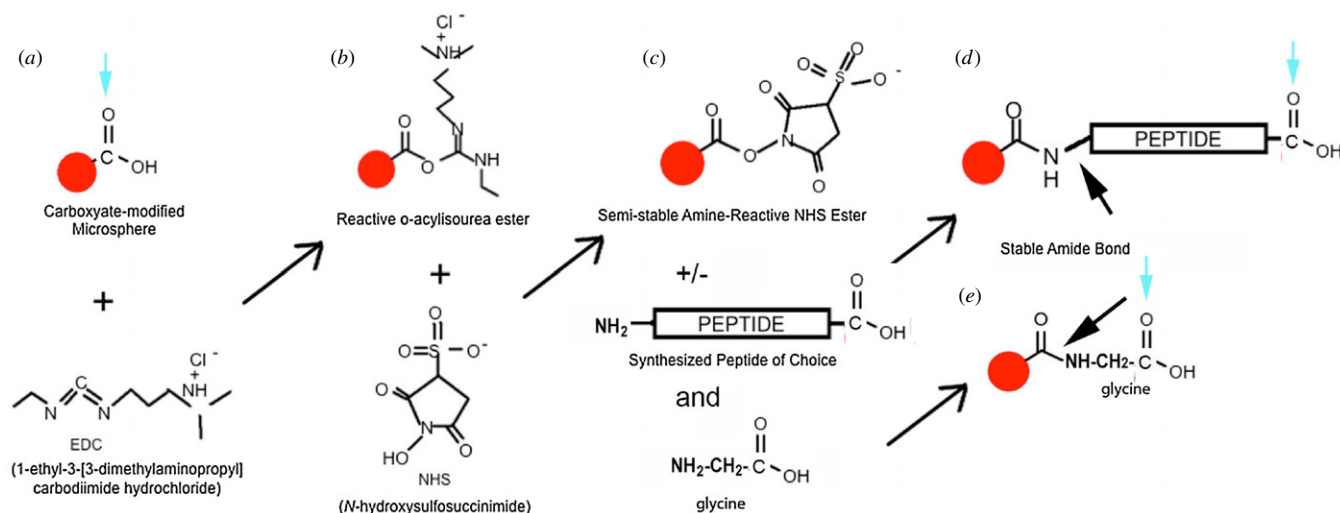
Figure 1. Diagram of conjugation of COOH-beads to peptides showing orientation of peptide relative to the bead and display of COOH moieties in the final products. Carboxylated microspheres are activated by EDC (*a*) to create the reactive species: beads with an o-acylisourea ester (*b*). Addition of free N-hydroxysulfosuccinimide (NHS) converts the reactive ester to a semi-stable amine-reactive NSH ester (*c*), which leads to a subsequent reaction with primary amines on amino acids to produce a stable amide bond (*d*). When peptides are included in the final reaction, the beads are coated with the peptide, and any remaining activated groups on the beads quenched with glycine. When peptide is omitted (*e*), the activated beads are cross-linked only to the glycine. When ethanolamine is included, the conjugation results in an amide-linked hydroxyl instead of carboxyl group (not shown). Note that in all cases the carboxyl group will be displayed on the surface (blue arrows), including in the case of the single amino acid glycine. Thus the orientation of the peptide on the beads is similar to that of the whole protein inside cells. Also note that while only one reaction is diagramed, each of the millions of COOH moieties on the beads participates and is conjugated when peptide concentrations are tenfold saturating. Also see figure 1.1.5 from *Invitrogen* introduction to amine modification (http://www.invitrogen.com/site/us/en/home/References/Molecular-Probes-The-Handbook/Fluorophores-and-Their-Amine-Reactive-Derivatives/Introduction-to-Amine-Modification.html, and Thermo Scientific Pierce Protein Research http://www.piercenet.com/browse.cfm?fldID=02030312).

Biological Laboratory at Woods Hole, MA, as described (Bearer *et al* 2000, 1993, DeGiorgis *et al* 2002, Satpute-Krishnan *et al* 2003). Squid do not live for any length of time in captivity. Hence, axons must be dissected and used for experimentation within 24–36 h after catch from the North Atlantic. The distal end of the axon is tied with fine silk thread while the giant ganglion at the proximal end is retained with the specimen. Thus orientation of the axonal polarity is preserved and easily discerned. After initial dissection from the animal, the axonal sheath is removed under a dissecting scope taking care not to damage the axonal membrane. The axon is then transferred to a microscope slide with a 1 mm × 2 cm × 1 cm piece of Teflon on one side to stabilize the axon along its length on one side against the pressure of the injection needle which is inserted laterally on the opposite side. Injection is performed under direct observations in a Zeiss upright axioscope microscope (Carl Zeiss, AG, http://www.zeiss.com/microscopy) equipped with a Narishige micromanipulator (Narishige International USA, Inc., East Meadow, NY, http://www.narishige.co.jp/english) and a syringe-based injection apparatus (Jaffe and Terasaki 2004) using a 10× objective containing a micrometer eyepiece to measure lengths of injectate in the micropipette and diameter of the extruded droplet as measured with the eyepiece to calculate volume injected.

Micropipettes were drawn from 1 mm Quartz capillary tubes (Sutter instruments, Novato, CA) on a Narishige PC-10 micropipette puller, back-filled with 1 μL of Hg using a 10 μL Hamilton syringe, and front-loaded with ~1500 pL

of fluorescent beads at $\sim 4 \times 10^{12}$ beads/mL. For co-injections equal volumes of red and green fluorescent beads (1:1 suspension) were mixed by trituration before loading into the micropipette for injection. The bead suspension was capped at both ends with dimethylpolysiloxane oil (Jaffe and Terasaki 2004), which was co-injected before and after the suspension to serve as a stable marker of the injection site also visible by phase microscopy in the confocal microscope for rapid identification of the injection site.

After injection, axons were transferred to a chamber containing Ca^{2+}-free seawater with no. 1 coverglass spacers and covered with a no. 1 coverslip for imaging in a Zeiss inverted 510 laser scanning confocal microscope (LSM 510). During imaging, viability of axons is monitored at each step by observing the stability of oil droplets and continued transparency of the axoplasm (Bearer *et al* 2000, Satpute-Krishnan *et al* 2003, 2006). We also sometimes monitor mitochondrial movements using R123, a membrane permeable dye that fluorescently labels metabolically active mitochondria and reveals both activity of transport and health of the axon (Satpute-Krishnan *et al* 2003).

Imaging axonal transport by confocal microscopy

The thickness of the axon (0.8–1.0 mm) requires long-working-distance objectives to image deep enough to witness transport. Movements of fluorescent beads in the giant axon were therefore collected with 10× Zeiss Plan Neofluor 0.3 NA Air (5.5 mm working distance), and 40× Zeiss

Table 1. Bead types and peptides.

Peptide	Position	Amino acid sequence	Charge	pI	Transport
hAPP-C	681–695	GYENPTYKFFEQMQN	−1	4.29	Yes
sAPP-C	598–612	GYENPTYKYFE-MQN	−1	4.29	Yes
hAPP-JMD	647–665	KKKQYTSIHHGVVEVDA	+3	8.60	No
sAPP-JMD	565–582	KRRTQRQRVTHGFVEVDP	+4	11.89	No
hAPP-CMID	666–681	AVTPEERHLSKMQQN	+1	7.01	No
sAPP-CMID	583–597	AASPEERHVANMQMS	−1	5.30	No
Jumbled hAPP-C	Derived from 681–695	GEPYFEMNYNTKFQQ	−1	4.29	No
Negatively charged	–	–	−1	5.0	Yes
Glycine	–	G	−1	5.97	No
Ethanolamine	–	–	0	7.0	No

h, human, numbers are for human neuronal APP isoform, s, squid sequence.
Human APP695 (NCBI UniGene code Hs.434980).
Squid APP (GenBank accession no. DQ913735).

Achroplan 0.8 NA Water Correctible (3.6 mm working distance) objectives with phase rings.

Green and red fluorescence and phase images were collected simultaneously using the multi-tracking option on the Zeiss LSM 510. Images were collected at 4 s intervals. This capture interval was later proven to be optimal for subsequent bead tracking, and was calculated based on the rate of translocation of the beads and their size with the 40 × objective (Vermot *et al* 2008). Image series were obtained in three channels, with the Argon laser (488 nm) to excite green fluorescent microspheres and the helium–neon laser (543 nm) to excite red fluorescent microspheres. Phase was used to obtain background images of the full-thickness axon that were later used to align the images in the sequence according to their gray-scale intensity maps. The alignment was then applied to the companion fluorescence images in the sequence (Satpute-Krishnan *et al* 2006). Alignment is necessary for analytical processing to obtain precise measurements of biophysical properties of the movements of cargo. Image sequences were converted from Zeiss .Ism into tiff stacks and figures were prepared using Photoshop (Adobe Systems, San Jose, CA).

Biophysical measurements of bead behavior

After application of time stamp and magnification bar, images sequences were exported from LSM format to a tif sequence and then imported into MetaMorph 7.0 r1 (Molecular Devices, LLC). First the sequence is aligned using MetaMorph 'align stack' routines, with manual correction of each image based on its gray scale intensity pattern overlap to its nearest neighbor in the phase microscopy channel on a frame-to-frame basis. Instantaneous velocity measurements were obtained from the displacement of individual beads using the MetaMorph tracking option, which generates a spreadsheet in Excel (Microsoft). Beads were selected at random with the limitation that the trajectory did not overlap with other beads. Only beads that moved into and out of the frame were included for velocity calculations to reduce the chance of including short pauses occurring between frames. Pauses were defined by instantaneous velocities below 0.1 μm, as this is too small to measure accurately. Frequency of bead movements was calculated by selecting a region of interest in the video that contained approximately 100 beads, counting the beads in the first frame, and then the number of streaks in each set of 10 superimposed consecutive frames (streaks represent movement). For non-motile beads, it was difficult to find regions with 100 beads that were not overlapping, since most of these remain within the bolus in the injection site. Automated kymographs were performed on 1–4 pixel wide selections across the path of the beads using MetaMorph. Statistical comparisons were performed in Matlab using the statistics toolbox (MathWorks, Natick, MA).

Magnetic bead pulldowns

Carboxylated magnetic beads (100 μL, 2.0 × 10⁹ mL⁻¹, of 1 μm diameter magnetic beads) (Dynal, Life Technologies, Grand Island, NY) were conjugated with 20 μL of peptide stock (25 mg mL⁻¹) according to the same protocol as for fluorescent beads except instead of washing in the microcon tube, beads were collected with a magnet and washed by repeated removal and replacement of buffer. In addition to the human APP-C peptide, we also tested squid APP-C and two other peptides derived from the cytoplasmic domain of human or squid APP that were not motile (table 1) (Satpute-Krishnan *et al* 2006). To estimate charge of the conjugated beads, we assigned a value of −1 to each acidic residue (Asp (D), Glu (E), and the c-terminal carboxylic acid; a value of +1 to each basic residue (Arg (R), Lys (K), His (H)). We then calculated the overall predicted charge of the bead-peptide conjugate. The pI was estimated using MacVector (Accelrys Inc., 2004). For conjugates with a pI < 6.5 we considered the charge to be −1 in the axon, where the pH has been calculated as 6.85 (Schnapp and Reese 1989, Schnapp *et al* 1992, Schroer *et al* 1988). Collection of beads with a magnet instead of by centrifugation minimizes the possibility of non-specific co-sedimentation of un-bound material with the beads.

Axoplasm (35–50 μg protein/μL) extruded into 'buffer A' (motility buffer (Bearer *et al* 1993, DeGiorgis *et al* 2002, Satpute-Krishnan *et al* 2006)) with 1% Triton X100, 1/100 dilution of protease inhibitor cocktail, and 5 mM DTT (Bearer *et al* 1993) was diluted to 400 μL with motility buffer plus 0.1% Triton, clarified by centrifugation, and incubated with beads. Pieces were cut from frozen rat brains (∼0.4 g) (Pelco, Clovis CA), weighed, and then homogenized in 'buffer B' (50 mM Tris pH 6.8, 50 mM KCl, 100 mM NaCl, 2 mM

CaCl$_2$, 2 mM MgCl$_2$, 1/100 protease inhibitors and 5 mM dithiothreitol) and 1% Triton. After centrifugation for 15 min at 15 000 g, extract was diluted to 10 μg μL^1 protein with buffer B plus 0.1% Triton and 1% BSA. Beads were incubated with extracts on a rotator for 1 h at room temperature, collected with a magnet and supernatant removed. Proteins in the supernatant were collected by precipitation in 10% tricholoracetic acid. Beads were further washed by three changes of buffer, and then beads and precipitated supernatants were resuspended in 20 μL of gel sample buffer made with un-buffered TRIS (pH 10.0) with careful accounting to maintain equivalent volumes.

Blots loaded in parallel with equal amounts of starting material, beads and equivalent volumes of supernatant were probed with primary antibodies (monoclonal anti-kinesin heavy chain antibody, (Chemicon, AB1614, Millipore, Billarica, MA) (Pfister 1989), pan anti-actin antibodies (Cytoskeleton, Inc., Denver, CO; CalBiochem, Merck Chemicals, San Diego, CA; Chemicon, Millipore, Billarica, MA; Sigma-Aldrich Chemicals, St Louis, MO), and anti-tubulin (Amersham, GE Healthcare, Piscataway, NJ) in Tris-buffered saline with 0.2% Tween+3.0% milk, then washed, incubated for 45 min with horseradish peroxidase conjugated secondary antibody (Chemicon, Milllipore, Billarica, MA) and bands detected by enhanced chemiluminescence (Amersham, GE Healthcare, Piscataway, NJ). Blots were stripped with 62.5 mM Tris-HCl (pH 6.7), 2% SDS, 100 mM 2-mercaptoethanol at 50 °C, followed by quenching of any residual HRP activity with 10 min in 0.2% Na-azide if reprobed. Alternatively to probe for more than one antigen, blots were cut horizontally across lanes such that each horizontal strip contained the molecular weight species expected of each antigen (kinesin heavy chain, actin or tubulin), and then each strip probed in parallel across multiple lanes from the same gel-blot. Strips were reassembled in the film cassette and the chemiluminescent signal developed with successive time points from 20 s to overnight onto x-ray film (Kodak). Film was developed in an automated Kodak X-Omat 1000A automated film developer.

A digital version of the resultant x-ray film was captured in a BioRad GelDoc and bands in the digital image measured computationally using freeware package from NIH, ImageJ 1.43 (http://rsbweb.nih.gov/ij/). To obtain a standard scale correlating recombinant kinesin heavy chain amounts with blot intensity and determine endogenous KHC concentrations in brain extract and axoplasm. Purified recombinant kinesin-1 heavy chain (rKHC) (Cytoseleton, Inc., Denver CO), which lacks part of the tail domain and thus runs at 70 kDa instead of the full length 124 kDa, was loaded in increasing amounts (2, 5, 10, 15, 20 μg mL^{-1}) and run in parallel with different volumes of axoplasmic or brain extract (2, 4, 8, 10 μL). Intensities of bands for rKHC were calculated as molar amounts of the dimer, as KHC is a dimer in the holoenzyme. The volumes described above typically produce extracts of both brain and axoplasm containing from 0.5 to 2.0 μmolar kinesin, consistent with previous reports that the concentration of KHC in axons is 0.5 μM (Brady *et al* 1990).

The ratio of bead-bound KHC (i.e. that in the bead pellet) to free KHC (i.e. that in the supernatant) was calculated

Table 2. Definitions of symbols used in mathematical model.

Variable	Definition
s, t	Distance and time coordinates
ρ_0, ρ_1	Linear density of immobile and mobile cargo
ρ	Total linear density of cargo
v_1	Instantaneous velocity of cargo beads
k_0, k_1	Attachment/detachment rates
D	Dispersion coefficient
$\langle v \rangle$	Cumulative velocity

from band intensities in blots of gels loaded with different amounts of pellets and supernatants from the same pulldown experiment and processed in parallel on the same blot. Multiple duplicate experiments and exposures were analyzed. Dissociation constant and Bmax were estimated by fitting the binding curve to the 'one site binding equation' <Y = Bmax/(Kd+X)> in Prism 4 software from GraphPad.

Mathematical model

Here, we outline the traffic model of Smith and Simmons (2001) which we used to describe the transport dynamics of an ensemble of mobile and immobile cargo within the axon. Transport of a single species of cargo in the axon is governed by the traffic equations:

$$\frac{\partial \rho_1}{\partial t} + v_1 \frac{\partial \rho_1}{\partial s} = k_0 \rho_0 - k_1 \rho_1, \tag{1}$$

$$\frac{\partial \rho_0}{\partial t} = -k_0 \rho_0 + k_1 \rho_1, \tag{2}$$

where s is distance traveled by the beads, t is time, ρ_1 and ρ_0 are the densities of mobile and immobile cargo beads, respectively, v_1 is the average instantaneous velocity of the mobile cargo beads, and k_0 and k_1 are the rates of attachment and detachment of cargo beads to and from microtubules. The symbols used in the model are listed in table 2. For the initial conditions, we consider all of the particles at $s = 0$, corresponding to a Dirac delta function. These initial conditions describe the experiment, where the trajectories of selected particles at different locations within the plume are measured relative to their initial location where the measurements for a particular bead were started. Smith and Simmons (2001) included additional terms in equations (1) and (2) associated with molecular diffusion; however, Brownian motion was not apparent in our video microscopy experiments and was thus omitted in our analysis.

At long times, defined by,

$$t \gg (k_0 + k_1)^{-1}, \tag{3}$$

the solution of equations (1) and (2) tends to a traveling Gaussian distribution centered around the moving frame, $s = \langle v \rangle t$ (Smith and Simmons 2001):

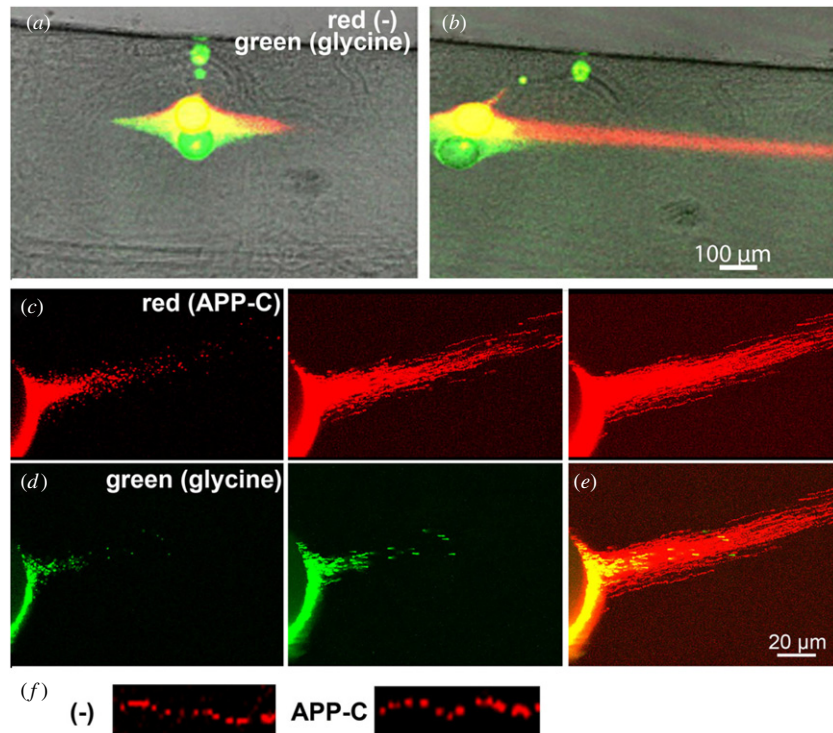$$\rho = \frac{e^{-\frac{(s - \langle v \rangle t)^2}{4Dt}}}{\sqrt{4\pi D t}}, \tag{4}$$

Figure 2. Relative transport of negatively charged, APP-C and glycine beads in the squid giant axon. (*a*) A low magnification image immediately after co-injection of red negatively charged and green glycine-conjugated beads showing the injection site, marked with an oil droplet, appearing as a round yellow sphere. Overlap of red and green fluorescence produces a yellow image. Supplementary video S1 (available from stacks.iop.org/PhysBio/9/055005) shows movements imaged at 10× immediately after injection. (*b*) At 50 min after injection, the red carboxylated beads have progressed in the anterograde direction (to the right) while the green glycine-conjugated beads have made no progress. (*c*)–(*e*) An axon co-injected with red APP-C beads and green glycine beads and imaged for 100 frames at 4 s intervals at 40× magnification. (*c*) Red channel (left) first frame; (center) 50 frames superimposed; (right) all 100 frames superimposed. Note the progression of individual beads towards the right, anterograde, side of the injection site heading towards the presynaptic terminal. (*d*) Two images of the green channel from the same video sequence; (left) first frame; (center) 100 frames superimposed. Note the lack of significant movement of the green glycine beads. (*e*) Both red and green channels from 100 frames superimposed of the same video as in (*c*) and (*d*). (*f*) Single bead trajectories at high magnification from a set of superimposed frames showing movements of beads. See supplementary videos S2 and S3 for video sequences at high magnification of negatively charged (−) beads and supplementary video S4 for APP-C beads (available from stacks.iop.org/PhysBio/9/055005).

where $\rho = \rho_0 + \rho_1$ is the total linear density of the beads normalized by the total quantity of cargo beads, $\langle v \rangle$ is the cumulative (average) velocity of the cargo given by

$$\langle v \rangle = \frac{k_0}{k_1 + k_0} v_1, \tag{5}$$

and D is the dispersion coefficient,

$$D = \frac{k_1 k_0}{(k_1 + k_0)^3} v_1^2. \tag{6}$$

Accordingly, the cumulative distribution of cargo beads at long times (3), obtained by integrating equation (4), is given by

$$\frac{1}{2}\big[1 + \mathrm{erf}(\eta(s,t))\big], \tag{7}$$

where $\mathrm{erf}(\eta)$ is the error function and $\eta(s, t)$ is the combined (similarity) variable,

$$\eta(s, t) = \frac{s - \langle v \rangle t}{\sqrt{4Dt}}. \tag{8}$$

Although molecular diffusion is omitted from equations (1) and (2), dispersion nonetheless arises from the stop and go dynamics of the cargo beads. Below, we compare the cumulative distributions of cargo positions based on equations (4)–(6) to those obtained from our experiments. Finally we

show that formula (8) can be used to predict the behavior of specific cargo at much longer times than is readily observed experimentally.

Numerical analysis was performed using Fortran, and graphs were generated in gnuplot. Data analysis was performed using Excel, MatLab and some customized Fortran code with graphic representation via gnuplot and figures produced using Adobe Photoshop.

Results

Carboxylated negatively charged beads and beads conjugated with the 15-amino acids of the APP-C but not with glycine are transported after injection into the squid axon.

Fluorescent beads conjugated to a peptide derived from the APP-C moved rapidly in the anterograde direction after co-injection into the axon with glycine-conjugated immobile beads, as we have previously described for APP-C beads when co-injected with beads conjugated to other inert APP peptides (Satpute-Krishnan *et al* 2006). Here we show that qualitatively similar behavior is observed for carboxylated (negatively charged) beads (figure 2 and supplementary videos 1–4

(available from stacks.iop.org/PhysBio/9/055005). In contrast, beads conjugated to a single amino acid, glycine, that also display a carboxyl group on their surface but with only one intervening amine (see figure 1 for orientation of conjugates on the bead surface) were 'dead in the water'—only marginal transport was observed when either co-injected with rapidly motile negatively charged beads (figures 2(*a*) and (*b*)) or with APP-C peptide-conjugated beads (figures 2(*c*)–(*e*)). When multiple frames from a time-lapse movie are superimposed, the tracks of individual beads are readily appreciated (figures 2(*c*)–(*e*)). Displacement of the beads between frames is used to calculate their instantaneous velocities (figure 2(*f*)).

Since both negatively charged and APP-C beads apparently transport similarly, we analyzed whether APP-C might interact with motors merely on the basis of charge. Indeed APP-C and negatively charged beads have the same ionic charge at neutral pH (−1) (table 1). However, several other peptides, including one with the same amino acid sequence as APP-C but in a different order, were not actively transported in the axon even though they had a charge similar to that of transported beads (table 1) (Satpute-Krishnan *et al* 2006). Thus neither the ionic charge nor the presence of the COOH group on the bead correlates with its ability to be transported. For negatively charged beads, the density of COOH groups together with ionic charge on the bead surface may explain enhanced ability as compared to glycine or peptide conjugates. These two new bead types, negatively charged (COOH) and glycine, provide positive and negative controls respectively for peptide-mediated transport.

In the giant axon, two biological factors make such controls mandatory. First, because the squid are wild-type and die quickly in captivity, a positive control that reliably transports in living axons is necessary to confirm viability of the axon and preservation of transport capacity. Second, injury to the axon can produce a phenomenon known as axoplasmic streaming, in which the particulate contents of the axon move at fast transport rates but by a contraction of the sheath and other actomyosin-based movements and not by motor-driven transport. An inert bead that is not transported serves to report on the integrity of the axoplasm and the absence of this non-specific streaming. When screening other candidates for motor receptors, it will be crucial to have in hand a non-peptide-based cargo, such as these negatively charged beads, to validate transport capacity of the axon in the case when a candidate fails to move; and an inert bead to validate transport rather than streaming in the case when the candidate does move.

Next we sought to determine what, if any, differences exist between the transport efficiency of APP-C-conjugated as compared to carboxylated—negatively charged—beads. Our hypothesis was that a peptide binding to motors would be more specific with higher affinity than negative charge alone but it was unclear how binding specificity would affect bead transport. To quantitatively compare bead movements, we measured their biophysical parameters with respect to cumulative and instantaneous velocities, and pause and run durations. Multiple beads transporting in at least three different axons for each bead type were recorded and representative beads measured. Cumulative results were statistically analyzed
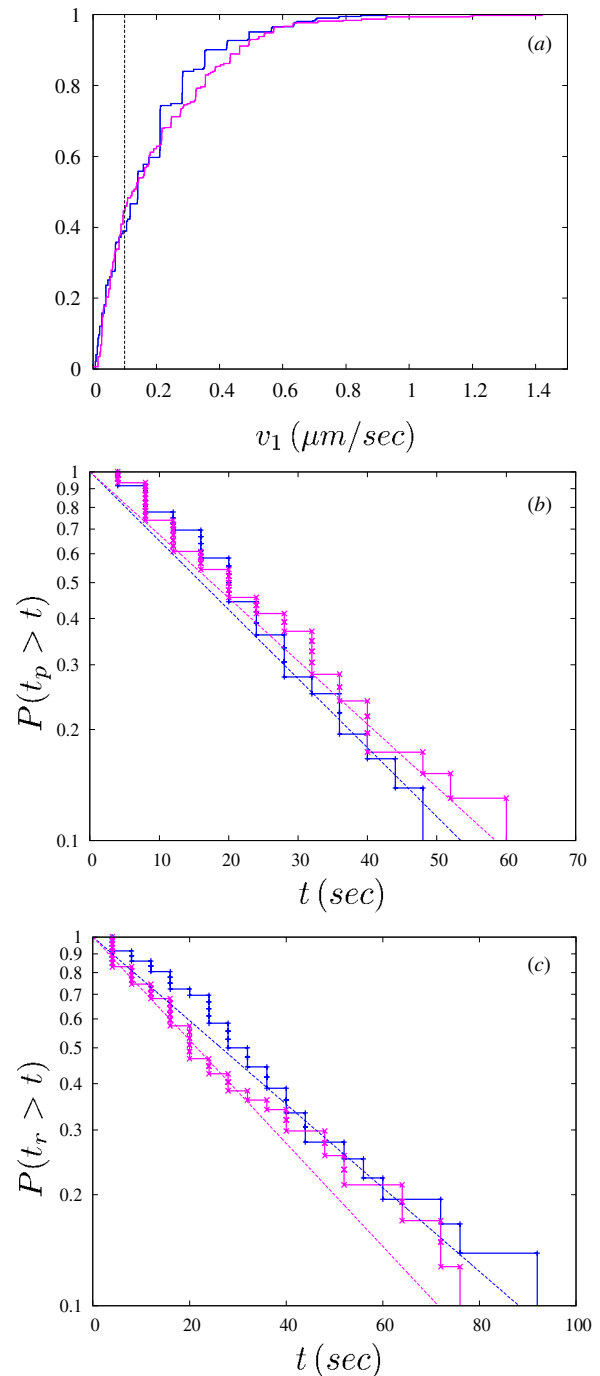

Figure 3. Quantitative analysis of bead behavior. Cumulative distributions for the instantaneous velocities (*a*); negatively charged beads (blue line) and APP-C beads (pink line) obtained from displacements between successive video frames (available from stacks.iop.org/PhysBio/9/055005). Runs are defined by $v_1 > 0.1$ (dashed line). Probability distributions for pause times (*b*) and run times (*c*) for negatively charged beads (blue lines) and APP-C beads (pink lines). Experimental measurements (solid lines), Poisson distributions equation (9) corresponding to the attachment/detachment rates defined by equation (9) (dashed lines).

for APP-C and negatively charged beads. The results are shown in figure 3 and summarized in table 3. Despite the binding specificity of the APP-C beads relative to the negatively charged beads, the two bead types have similar distributions

Table 3. Mean values for the instantaneous velocity and attachment and detachment rates for negatively charged and APP-C beads extracted from the distributions depicted in figure 3. The run length is obtained from the instantaneous velocity and detachment rate as v_1/k_1.

	Instantaneous velocity	Attachment rate	Detachment rate	Run length
Cargo type	v_1 (μm s^{-1})	k_0 (s^{-1})	k_1 (s^{-1})	(μm)
Negatively charged	0.279	0.0431	0.0261	10.7
APP-C	0.371	0.0394	0.0322	11.5

of pause and run durations (figures 3(*b*) and (*c*)). However, the APP-C beads have a higher instantaneous velocity (figure 3(*a*)) and are thus transported more rapidly than the negatively charged beads as will be shown.

The distributions of the instantaneous velocity shown in figure 3(*a*) were obtained by measuring the bead displacements, $\Delta s = \sqrt{\Delta x^2 + \Delta y^2}$, between video frames (4 s intervals) (available from stacks.iop.org/PhysBio/9/055005). Here we take account of two-dimensional (*x* and *y*) displacements in the field of view to allow for variations in alignment of microtubules relative to the field of view in the images. The distributions of pause and run durations depicted in figures 3(*b*) and (*c*) were obtained by defining pauses as displacements characterized by instantaneous velocities v_1 below the critical value $v_1 < 0.1$ μm s^{-1}. Similar criteria have been used previously (e.g., Brown *et al* 2005). The mean value of the instantaneous velocity, given in table 3, is the arithmetic mean of the restricted portion of the distribution given in figure 3(*a*) corresponding to $v_1 > 0.1$ μm s^{-1}.

The distributions of pause and run times depicted in figures 3(*b*) and (*c*) are consistent with a Poisson distribution

$$P(t) = \mathrm{e}^{-kt}, \tag{9}$$

where $P(t)$ is the probability of a pause/run duration greater than t, and the exponent k is obtained from the average pause/run time according to the formula,

$$k^{-1} = \int_0^\infty P(t)\,\mathrm{d}t. \tag{10}$$

Values for the attachment/detachment rates thus obtained are listed in table 3. The dashed lines in figures 3(*b*) and (*c*) correspond to Poisson distributions (9) with rates defined by equation (10). Note that the distributions of pause and run durations and the attachment/detachment rates derived from them are sensitive to the criterion used to define pauses and runs (i.e. the critical value of the instantaneous velocity).

Another key parameter in biophysical analyses of bead movements, useful for comparisons of the behavior of different cargo, is the frequency that beads within a population move (figure 4). In our previous report (Satpute-Krishnan *et al* 2006),
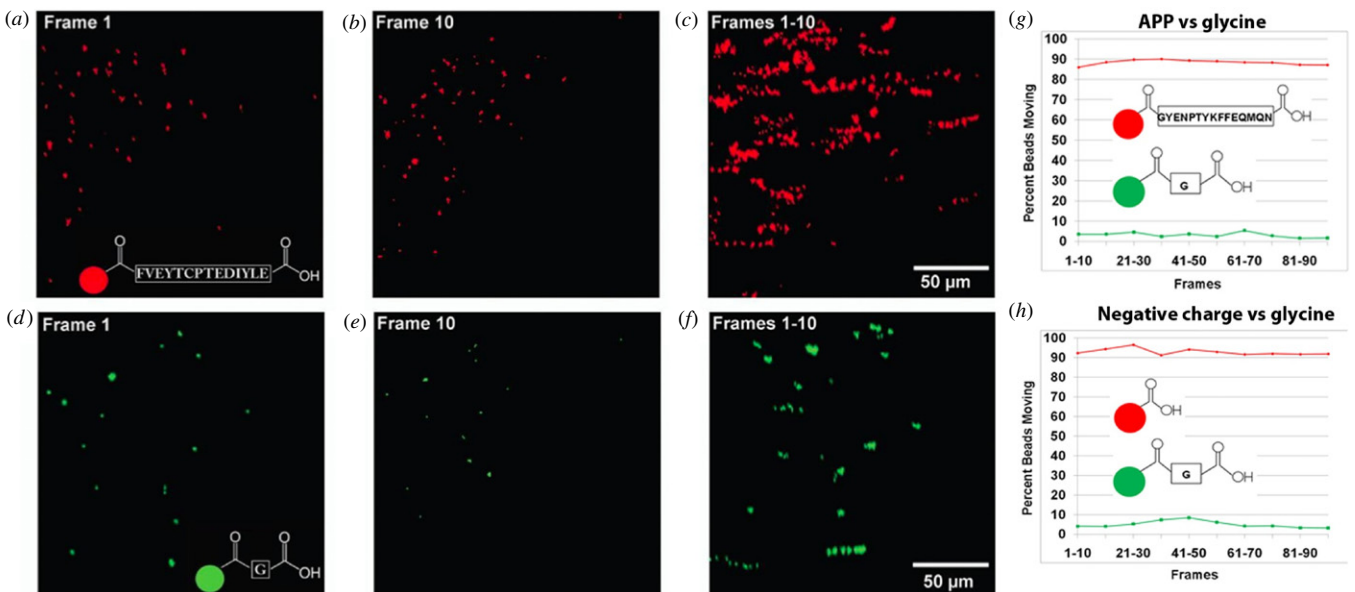

Figure 4. Method to measure frequencies of bead movements. (*a*)–(*c*) Red peptide beads, and (*d*)–(*f*) green glycine beads in an axon co-injected with red APP-C and green glycine beads demonstrating the method for counting the ratios of moving and stationary beads across 10 frame segments. Top panels show the red channel (*a*) single frame 1; (*b*) single frame 10; and (*c*) stacked frames 1–10 stacked of beads. Dotted pathways in (*c*) represent beads moving during the 10 frames. (*d*) Green channel showing individual frame 1; (*e*) individual frame 10; and (*f*) frames 1–10 of glycine beads. Minimal numbers of dotted lines in (*f*) indicate rare glycine bead movement over these ten frames. Measuring the distance between the dots also allows determination of the velocity of bead movement. (*g*) Graph showing results of per cent of beads moving in each 10-frame segment of a 100-frame video captured at 4 s intervals after co-injection with APP-C (red line) and glycine (green line) beads (available from stacks.iop.org/PhysBio/9/055005). (*h*) Graph showing results of percent beads moving in an axon co-injected with carboxylated (red) or glycine conjugated (green) beads. When co-injected with non-motile beads, both APP-C beads and carboxylated beads appear to behave similarly.

we focused on whether the APP-C beads moved at all. Now we report two types of beads that move, APP-C conjugated and negatively charged beads, and hence our focus changes here to whether transport is the same for all cargo, or if these two beads displayed any differences in behavior. We developed a new method to compare bead movements: Frequency of moves. We counted how many beads of the total were moving in any 10 frame sequence.

To quantify the ratio of moving to stationary beads in a window of time, we superimposed 10 frames captured at 4 s intervals at 10 frame intervals over a 100-frame video, giving 10 data points per video using MetaMorph 'stack arithmetic' routine (figure 4). Superimposition of frames allows us to count the number of beads in the first frame, and compare to the number of tracks in the image of ten superimposed tracks. In the example shown in figure 4, the green beads are conjugated to a single amino acid, glycine, whereas the red beads were conjugated to the 15-amino-acid APP-C peptide. Qualitatively a distinct difference in the number of tracks in the red and green channels after 10-frame superimposition is obvious. When the quantitative results are graphed, we immediately see that either APP-C or negatively charged beads sustain motility throughout the duration of the imaging with 70–90% of the beads moving in any given 10-frame segment from beginning to end of the sequence. In contrast, glycine-conjugated beads never achieve more than 10% motility throughout the recording time. This finding was consistent for all axons, remained throughout the imaging time, and was not affected by distance from the injection site.

APP-C peptide pulls down kinesin-1

The velocity of movement of the APP-C conjugated beads is suggestive of a kinesin-type microtubule motor. Kinesin-1, also known as conventional kinesin, is soluble and abundant in the axon, estimated at 0.5 μM (Brady *et al* 1990), and thus would be available to bind to exogenous cargo such as our beads. Previous binding studies found that recombinant full-length C-terminus of APP tagged with GFP binds to recombinant GST-tagged kinesin light chain with an affinity of approximately 16–18 nM for KLC1 and 2, respectively (Kamal *et al* 2000). In a subsequent publication another group using a different immunoprecipitation strategy initially reported that such direct binding was not reproducible (Lazarov *et al* 2005). Synaptic vesicles also bind purified kinesin-1 (Sato-Yoshitake *et al* 1992) with similar affinity, 18 nM.

In our previous studies, we reported that APP-C peptide from either squid or human was capable of mediating bead transport, although the peptide derived from the squid amino acid sequence, which differs by two amino acids from human, displayed a slightly faster average instantaneous velocity in the squid axon (Satpute-Krishnan *et al* 2006). We also reported the curious finding that the full-length cytoplasmic domain of the human sequence, present in our recombinant C99 peptide, was 30% faster than the APP-C peptide, with slightly shorter pauses. Despite this, peptides other than APP-C derived from the cytoplasmic domain displayed no motility. One explanation for these results could be that the other

regions of the tail facilitate binding but do not bind sufficiently well on their own to mediate transport. Alternatively, display of the binding domain further from the bead surface might allow more motors and tighter binding without any specific contribution of the intervening sequences.

To test these alternatives and measure the binding affinity of the various peptides to kinesin-1 we performed magnetic bead pulldowns with each of the APP-derived peptides and probed for kinesin-1 (figure 5). Isolation of the beads through magnetic interactions rather than centrifugation allowed a less stringent solubilization extraction procedure with reduced possibility of non-specific co-precipitation of larger complexes. We used peptides derived from either squid (s) or human (h) APP (table 1), to pulldown proteins from either detergent solubilized squid axoplasm or rat brain extracts (figure 5). Extracts, magnetic bead pull-downs and their corresponding supernatants were probed for kinesin-1 with antibodies against the heavy chain (KHC), which recognizes a single band of the appropriate molecular weight ($\sim$124 kDa) in either rat or squid extracts (Brady *et al* 1990). We used rat brain to obtain some validation that our measurements obtained in squid axons would pertain to other, mammalian systems as expected for such highly conserved proteins.

Both APP-C peptides, with either human/rat or squid sequence, pulled down kinesin-1, clearing it from axoplasmic (figure 5(*a*)) or rat brain extracts (figure 5(*b*)). For any other peptide derived from the cytoplasmic domain of APP, kinesin-1 remained in the supernatant, which is consistent with the lack of motility of beads conjugated to these peptides (Satpute-Krishnan *et al* 2006) and demonstrates that the increased motility of the C99 protein is unlikely due to a separate binding domain in the tail. Actin, significantly more abundant in axons (Bearer and Reese 1999, Fath and Lasek 1988, Morris and Lasek 1984) than kinesin-1 (0.5 μM) (Morfini *et al* 2002), was found at low amounts in the pellets and serves here as a loading control. Corresponding gels stained for protein confirmed that extracts contained equivalent amounts of total protein and detected no other bands correlating with motility (not shown). Both human and squid APP-C peptides pulled down both squid and human kinesin-1, although the squid peptide may have slightly lower affinity for the rat kinesin.

Others have reported that kinesin-1 interacts with negatively charged beads (Terasaki *et al* 1995). In our pulldown assay, we were unable to detect sufficient binding of negatively charged beads with kinesin to perform affinity binding studies. Thus under the conditions of this assay, APP-C has a much higher affinity for kinesin-1 than negatively charged beads.

The affinity of the kinesin-1 motor complex for the APP-C peptide was determined by quantitative Western blotting of pulldowns from a series of concentrations of rat brain extract (figures 5(*c*) and (*d*)). First, a calibration curve of band intensity versus recombinant purified KHC (rKHC) concentration was observed by measuring the intensity of bands in blots of known amounts of rKHC. The amount of kinesin-1 in each brain extract was calculated by comparing band intensities with known amounts of rKHC probed on the same blot. Then pulldowns and corresponding supernatants from a series of dilutions of rat brain extract were probed in parallel and band
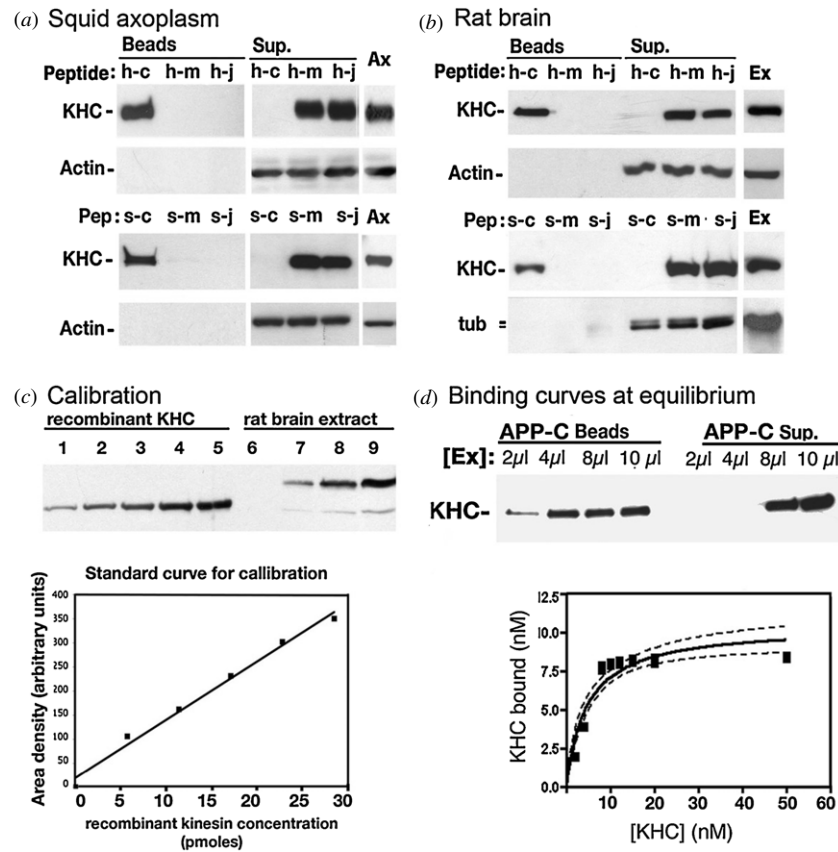
Figure 5. APP-C peptide binds kinesin-1 with high affinity. (*a*) Axoplasm: Pooled axoplasmic lysate (50 μL at 1 μl mL^{-1}) from five axons was incubated in parallel with a series of magnetic beads (20 μL) conjugated to six different peptides (20 μL of each at 25 mg mL^{-1}): h-c: human APP-C; h-m: human APP-C^{mid}; h-j: human APP-JMD; and s-c: squid APP-C; s-m: squid APP-C^{mid}; s-j: squid APP-JMD (see table 1 for pepide sequences). Ax: lane loaded with the same axoplasmic preparation used for the pulldown. (*b*) Rat brain: magnetic beads conjugated to the same peptides as in (*a*) were incubated with rat brain extract. Blots of beads and equal amounts of corresponding supernatants were probed for kinesin (KHC), actin and tubulin. (*c*) Quantification of kinesin-1 in extracts and calibration of KHC band intensity. Recombinant motor domain from human KHC (rKHC, top panel, left 5 lanes, loaded with 2, 5, 10, 15 and 20 μg) probed by Western blotting and imaged by chemiluminescence in parallel with rat brain extract (top panel, right 4 lanes, 2, 4, 8, and 10 μL of extract). The recombinant motor domain migrates at ~75 kDa whereas full-length endogenous KHC is ~124 kDa. Density of signal on the blot was determined using ImageJ scans of a digital image. Plot of area density in arbitrary units versus molar amount of recombinant kinesin displays linearity (lower panel). Shown is an example of kinesin standards for one brain extract. This analysis was performed for every extract used in pulldowns. In this instance, the extract contained 1.8 μM kinesin. (*d*) APP-C pulls down kinesin-1 with high affinity. Magnetic beads conjugated to APP-C peptides pulled down kinesin-1 (KHC) from rat brain extracts in a concentration-dependent and saturable manner. APP-C beads (20 μL) were incubated with a series of extract dilutions as indicated and beads and supernatants (sup) analyzed by Western blot for kinesin-1 (KHC). Binding curves (bottom panel) were obtained by plotting the data from 27 individual pulldowns and performing a nonlinear regression to obtain the best fit curve as described in materials and methods. Dotted curves indicate 0.05% confidence limits.

intensities measured (figure 4). The amount of kinesin-1 bound to beads was graphed against the amount of kinesin-1 in the extract to obtain a binding plot. Nonlinear regression analysis of this data yielded an estimated Kd of 4.7 $\pm$ 0.8 nM from a plot of 27 independent pull-down experiments. Thus the small 15 aa peptide has higher affinity in this assay than the full length cytoplasmic tail of APP for kinesin-1.

Qualitative comparisons of overall bead movements

Unbiased time–distance plots called kymographs, obtained by stacking a small (1–4) pixel horizontal band from each frame provide a quick reference for directionality, with the slope of the trajectory indicating speed (figure 6). Kymographs give an indication of pause frequencies and durations, as moving beads appear as oblique lines, and stationary beads are vertical. Small movements of the live axon during imaging may give some retrograde drift, obvious in a slight lean leftwards from the vertical for stationary beads. Conclusions from this qualitative analysis of a small number of beads for each motile species is the striking similarity of slope (velocity) for all moving beads in each kymograph. Pauses appear as intermittent vertical tracks in otherwise oblique lines. Frequency and duration of pauses and run lengths are also displayed for the small number of beads captured in the 3 or 4 pixel-wide bands.

More comprehensive analysis of these parameters can be obtained using software tracking tools, as we previously reported for APP-C co-injected with other APP-derived peptides (Satpute-Krishnan *et al* 2006), for herpesvirus transport (Cheng *et al* 2011, Satpute-Krishnan *et al* 2003) and
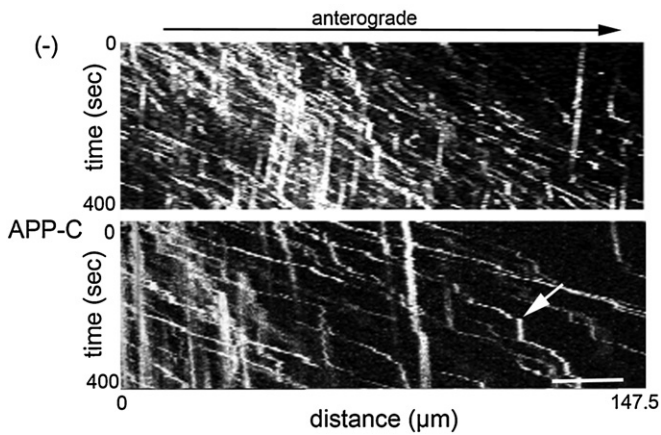
Figure 6. Kymographs also indicate velocities, run lengths and durations, and pause frequencies of negatively charged- and APP-C-bead movements. Representative time–distance plots (kymographs) from 3 and 4-pixel-wide horizontal swath of two 400 frame, 4 s time-lapse sequences. Negatively charged- (−) and APP-C beads after injection into the squid giant axon as indicated. Vertical lines are produced by stationary beads and oblique lines by moving beads. The angle of the slope of moving beads relative to stationary beads is an indicator of velocity, with faster-moving beads closer to horizontal. Pauses produce a vertical interruption of an oblique line, an example of which is indicated by the arrow. Slight retrograde angle in the vertical lines of the (−) beads is due to retrograde drift of the axoplasm in that video. Disappearing trajectories and fuzzy vertical lines are due to multiple beads coming in and out of focus during the recording. Magnification bar (lower right) = 20 μm.

now report here for COOH beads and APP-C co-injected with glycine-conjugated control beads (figures 3 and 4, table 3).

Quantitative comparisons of overall bead movements

Here we quantitatively analyze the bead transport and compare our experimental results to the predictions of the mathematical model of Smith and Simmons (2001). By analyzing approximately 10 bead trajectories for each type of bead, we obtained ensembles of approximately 40 pauses and 40 runs. Under the assumption that the pauses and runs are statistically independent events, we are able to construct a much larger number of independent, experimentally derived bead trajectories by random sampling alternately from the ensembles of pauses and runs obtained from our experimental measurements. We are thus able to perform a resolved statistical analysis of the cargo transport from ensembles of experimental pause and run events derived from approximately 2500 (negatively charged) and 3300 (APP-C) s of data. This approach is supported by the results depicted in figures 3(*b*) and (*c*) given that random, statistically-independent events obey a Poisson distribution (equation (9)). The deviations from a simple exponential decay of the probability distributions in the figure (dashed lines) appear to be mostly the result of sampling at finite (4 s) intervals. Rare events (e.g., *P* < 0.1), however, are not well resolved in our 40-event ensembles of pauses and runs. Thus, a Poisson distribution corresponding to the dashed lines in figures 3(*b*) and (*c*) was used to

account for events characterized by *P* < 0.1; however, the stochastic, experimentally derived trajectories generated by this procedure are insensitive to the exact value used for this cut-off.

Figure 7 illustrates stochastic, experimentally derived bead trajectories for both bead types generated from our ensembles of pauses and runs according to the procedure described above. Pauses are represented by the red segments of the trajectories and runs by the green segments, and the distinction depends on the criterion, which in our analysis is determined by $v_1 < 0.1$ μm s^{-1}, as discussed above. Comparing figure 7(*a*) (COOH) with figure 7(*b*) (APP-C) reveals that the APP-C beads move more rapidly than the negatively charged beads and display more dispersion. This qualitative conclusion is supported by the results shown in figures 8 and 9 and the transport parameters reported in table 4. These results were obtained from 1000 stochastic, experimentally derived bead trajectories. Experimental values for the cumulative velocity and dispersion coefficient were obtained from the relations

$$\langle v \rangle = \frac{\mathrm{d}\langle s \rangle}{\mathrm{d}t}, \qquad D = \frac{1}{2} \frac{\mathrm{d} < s- < s \gg^2}{\mathrm{d}t}, \qquad (11)$$

which attain constant values at long times, as seen in figure 8. The experimentally derived values, listed in table 4, were thus obtained from the slopes of the dashed lines in the figure 8; the theoretical values are given by equations (5) and (6). Comparing the parameter values in table 4, quantifies the picture conveyed in figure 7, i.e. the APP-C beads are transported more rapidly and undergo more dispersion than the negatively charged beads. Fair quantitative agreement between the experimentally derived values and theoretical predictions is obtained for the cumulative velocity and dispersion coefficient even though the theoretical model is based only on the average value of the instantaneous velocity and our data show broad distributions for this parameter, as seen in figure 3(*a*). Larger discrepancies between the predicted and observed values for *D* may reflect the fact that the dispersion coefficient is associated with fluctuations and is thus more sensitive to variations in v_1 and rare events (i.e. long pauses or runs) which are not well resolved by the current size of the dataset. In any case, the predicted dispersion coefficient is close enough to the experimentally derived values to support the assumption that Brownian motion has negligible effect on the bead transport.

The evolution of the spatial distribution of experimental derived bead trajectories is depicted in figure 9 and compared to the model output. At long times ($t \geqslant 250$ s^{-1}) the spatial distributions collapse onto a universal distribution when rescaled in terms of the similarity variable defined by equation (8) (cf figures 9(*c*) and (*d*)). The results depicted in figures 9(*c*) and (*d*) indicate that the long-time self-similar distribution obtained from the experimental data agrees closely with the theoretical distribution predicted by equation (7) (dashed black curve); for both systems (negatively charged and APP-C beads), the root-mean-squared error is approximately 1%. As expected, the spatial distributions corresponding to shorter times do not collapse onto the universal distribution (cf, insets of figures 9(*c*) and (*d*)).
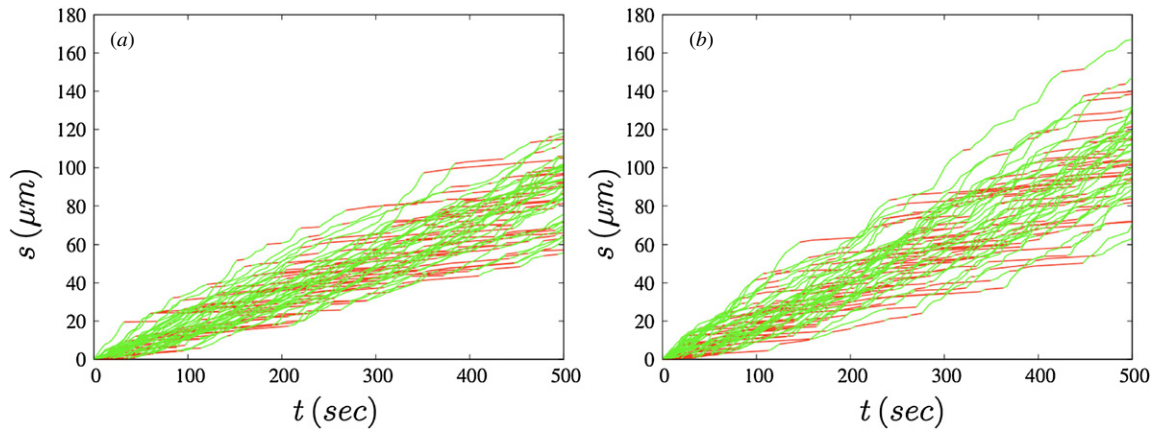
Figure 7. Stochastic trajectories of beads. 50 stochastic, experimentally derived trajectories for negatively charged beads (*a*) and APP-C beads (*b*) constructed by random sampling of experimental ensembles of runs (green segments) and pauses (red segments).
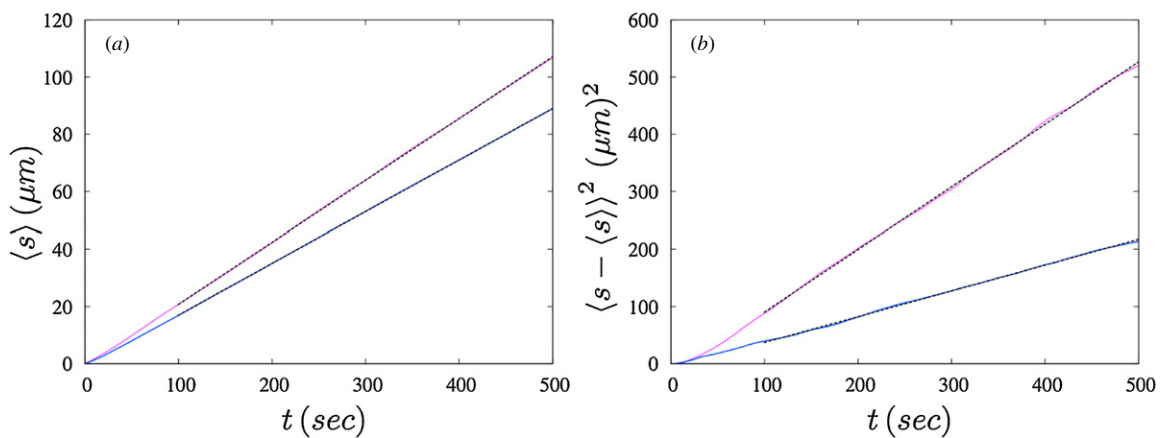

Figure 8. Evolution of bead position and variance. Evolution of the average position (*a*) and variance (*b*) obtained from 1000 experimentally derived trajectories for negatively charged beads (blue lines) and APP-C beads (pink lines). Cumulative velocities and dispersion coefficients given in table 4 were obtained from the slope at long times (dashed lines).

Table 4. Comparison of theoretical and experimental cumulative velocities and dispersion coefficients. Experimentally derived values obtained from slopes of mean position and variance (dashed lines, figure 8) according to equation (11); theoretical predictions given by equations (5) and (6) using parameters from table 3.

	Cumulative velocity, $\langle v \rangle (\mu\text{m s}^{-1})$		Dispersion coefficient, D ($\mu\text{m}^2 \text{ s}^{-1}$)	
	Experimentally derived	Theory	Experimentally derived	Theory
Negatively charged	0.180	0.174	0.22	0.26
APP-C	0.216	0.204	0.55	0.48

We obtained additional support for the model by comparing the cumulative distributions of the model's predicted output with actual bead displacements for each type of bead using experimentally derived $\langle v \rangle$ and D values (table 4). A Kolmogorov–Smirnov test (Andrews *et al* 2008, Massey 1951) showed that the model's prediction agreed with actual bead measurements both for negatively charged ($p = 0.96$) and APP-C ($p = 0.99$) at long times ($t = 156$ s).

Figure 10 contrasts the predicted evolution of negative charge and APP-C bead distributions at very long times. Here, we assume that the two bead types are independent, since in our experiments only one active bead type was injected into any particular axon. The results show that APP-C beads are transported significantly faster along the axon and undergo greater dispersion.

Discussion

Here we analyze the behavior of engineered cargo (negatively charged-, glycine- and APP-C-conjugated fluorescent nanospheres) after injection into the living axon of the squid, determine the affinity of the APP-C peptides from squid and human for the major microtubule-based motor, kinesin-1, in squid axoplasm and rat brain, and develop a mathematical model that predicts the dynamical behavior of APP-C-displaying cargo in axons.
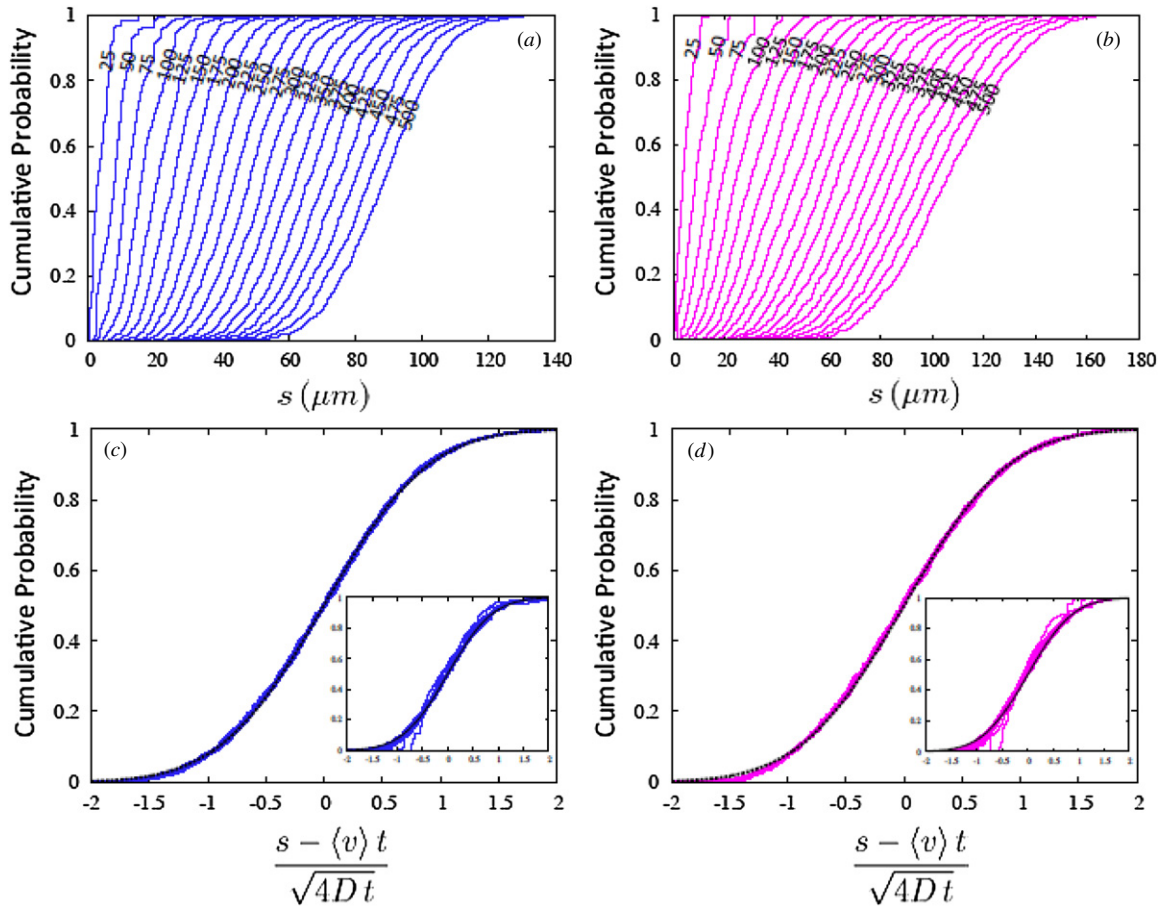
Figure 9. Cumulative spatiotemporal distributions. Evolution of cumulative spatial distribution for 1000 experimentally derived trajectories for negatively charged beads (*a*) and APP-C beads (*b*); time indicated in seconds ($t = 25-500$ s). Distributions for negatively charged beads (*c*) and APP-C beads (*d*) re-plotted using the similarity variable defined by equation (8) with experimentally derived values for the cumulative velocity and dispersion coefficient from table 4; model prediction given by equation (7) (dashed black curve); long-time distributions ($t = 250-500$ s) shown in main plot, all distributions ($t = 25-500$ s) shown in inset.
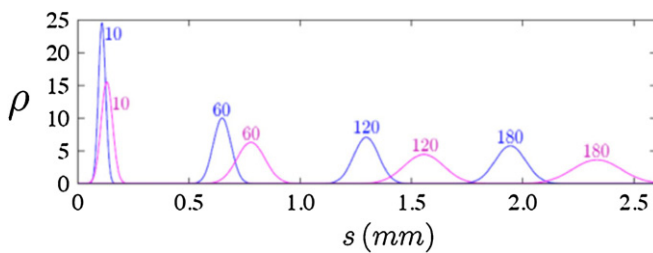
Figure 10. Predicted bead distributions at long times. Evolution of the spatial distributions of negatively charged (blue curves) and APP-C beads (pink curves) corresponding to the times indicated in minutes as predicted by equation (4) using the experimentally derived parameters for each bead type from table 4. The graph represents a superposition from two independent calculations. Note that at 3 h (180 min) the two distributions are almost entirely separate, with APP-C further along the axon.

The measurements reported here represent a close approximation to normal *in vivo* processes with some important exceptions. We exploit these differences to further our understanding of motor–cargo interactions. First, while our cargo displays a single species on the cytoplasmic surface, it is unlikely that biologically synthesized transport vesicles do. More likely endogenous vesicles display multiple species

of motor receptors capable of recruiting various cellular motors for transport. Thus our system is simpler than the natural situation. This simplicity of single receptor species on each bead allows us to observe the specific activity of that single species without confounding it with effects from other receptors, adaptors and enzymes. Information gained from this simple system can subsequently be integrated with a more complex model to predict competitions and synergies between receptors and, more significantly, between various types of vesicular cargo. Second, injection of a bolus of cargo at one location in the axon, which are in excess to the natural vesicular cargo, is not usual for endogenous organelles, which are primarily created in the cell body and progress at some constant rate(s) down the axon towards the synapse. We take advantage of the bolus to visualize movements of single particles from a known initiation site. While small numbers of our exogenous cargo would do little to the biochemical balance of motors and cargo receptors, in areas close to the initial bolus or areas through which many beads have already passed, exogenous cargo may out-number motors. We thus pay close attention to capturing images from the front of the beads advance at least 0.5 mm distal from the injection site.

In data we reported in 2006 (Satpute-Krishnan *et al* 2006), control beads were beads of a different color conjugated to

non-motile peptides, such as one derived from the *N*-terminal extracellular domain of APP and a jumbled peptide, with the same composition as the motile APP-C peptide in a different sequence. Here our control beads are conjugated to a single amino acid, glycine, such that they display the same carboxylic acid group to the cytoplasm without the intervening amino acids of the 15-aa peptide. These data definitively demonstrate that the COOH moiety at the terminus of peptides is not sufficient to mediate transport. Regardless of co-injected immotile bead species, comparisons between the model and the experimental data for the active beads yielded comparable results, thereby validating our squid axon model system.

The traffic-type mathematical model employed in our study depends on three parameters that were directly obtained by independent experimental measurements: the attachment and detachment rates of the APP-C coated and negatively charged beads, and the instantaneous velocity of the motile cargo. The fundamental assumption of the model that attachment and detachment rates for a given cargo bead are independent of its history, or equivalently that pause and run durations are statistically independent events, is supported by our experimental measurements. This finding allows the construction of a large ensemble of stochastic trajectories from a modest ensemble of experimental pause and run events. A statistical analysis of these trajectories validates the model prediction that the cargo distribution attains a self-similar Gaussian distribution that spreads by dispersion. The dispersion results from the attaching and detaching of cargo to the microtubules; Brownian motion appears to be negligible.

Other models for intracellular transport include Beeg *et al* (2008), Brown *et al* (2005), Jung and Brown (2009), Odell (1976). Such models have been based on very different data than ours. In the case of the Beeg *et al* model, the system is highly purified, with exact amounts of kinesin-1 passively adsorbed to beads that then are introduced into a chamber with stabilized purified microtubules and imaged by widefield illumination with analogue video at 22 semi-frames s^{-1} with 4–8-frame averaging while moving. In our case, motors are not pre-loaded on the bead—the bead must find and attach to the motor while inside the intact living cell. Beads must compete with invisible endogenous cargo for these motors, and there are quite likely to be several different species of motor in the axon. Because of the complexity of the intracellular environment, we visualized the bead movements by their fluorescence with laser-scanning confocal microscopy collecting time-lapse sequences with 1 s capture times and 3 s between frames (4 s time-lapse). Hence our averaged instantaneous velocity and our pause frequencies underestimate actual instantaneous speeds and pause frequencies. The behavior of negatively charged beads differs slightly from other *in vitro* reports, with respect to instantaneous velocity, as soluble factors from squid axoplasm support negatively charged bead movement on microtubules at an instantaneous velocity of 0.5 μm s^{-1} *in vitro* (Vale *et al* 1985b). Our experiments aim to discover the interaction of cargo receptors with transport machinery in the complex cellular environment, where at least three different anterograde motors (kinesin 1, 2 and 3) are found and competition between

disparate cargo receptors must occur. Our results differ from previous predictions, since instantaneous velocity seems to be more of a major factor in determining transport success for APP-C beads compared to negatively charged beads. It will be of significant interest to determine competition between different types of beads injected together into an axon.

Large bundles, 'plumes', of aligned oriented microtubules together with interwoven actin filaments are found in the deep axoplasm of the squid giant axon (Bearer and Reese 1999). These bundles are thought to provide the highways for microtubule-based transport, and lie closely enough together for vesicles or beads to travel from one to another during long-distance transport, unlike the reconstituted microtubule-based assays where microtubules are relatively distant one from the other. Rough calculations of the numbers of kinesin binding sites on our carboxylated beads show that only approximately 1000 kinesin-1 molecules would fit onto the surface area of each bead. Even with a million beads injected, there would still be significantly more kinesin-1 molecules in the axon then binding sites on the beads, according to our biochemical analysis shown in figure 5. Hence we assume that both types of beads under these conditions would have equal access to similar numbers of motors.

The mathematical model employed here represents a situation, like the experimental system, which is simpler than that which naturally occurs. The beauty of this experimental simplicity is that we can dissect the individual activities of specific receptors for their motors both biochemically and physiologically in the axon. Thus the mathematical model provides insight towards our central question: What, if any, differences exist between APP-C and negatively charged beads? Using the Smith and Simmons (2001) model we can predict how each type of cargo may contribute to the speed and ultimate success of reaching the nerve terminal or other destination. The validation of their model on both stochastic, experimentally derived trajectories and on raw bead data allows us to predict the position of cargo at much longer times that would be possible to image in the squid axon; an example is depicted in figure 10. The results in figure 10 show that at long, but experimentally accessible times, (e.g., 10 min), the distributions of the two bead types are predicted to be strongly overlapping, but the situation changes at very long (i.e. experimentally inaccessible) times. After 2 h, the predicted distributions of the two bead types are nearly separated with overlap only in the tails of the distributions; after 3 h, the predicted distributions are completely separated with the peak of the negatively charged bead distribution lagging the peak of the APP-C distribution by approximately 0.4 mm.

Thus deployment of the mathematical model provides biological information not possible with current experimental approaches. The mathematical model's simplicity, that is yet capable of predicting experimental outcomes, provides a framework upon which to develop more detail and complexity as we add parameters.

Future directions

These results provide a powerful starting point to develop more sophisticated assays for combinatorial motor-receptor

interplays, and for complex mathematical modeling of the dynamics between motor receptors and between vesicles with differing complements of receptors and motors.

Our assay and model reported here set-up a procedure to systematically identify other cargo receptors, and to quantify and predict competition between motors and cargo for transport efficiency. Such intracellular dynamics involving competitions between transported compartments and motor machinery are likely the underpinning for differentiation of subcellular compartments, and for differences in cellular morphology and function.

Acknowledgments

References

Allen R D, Allen N S and Travis J L 1981 Video-enhanced contrast, differential interference contrast (AVEC-DIC) microscopy: a new method capable of analyzing microtubule-related motility in the reticulopodial network of Allogromia laticollaris *Cell Motil.* **1** 291–302

Allen R D, Metuzals J, Tasaki I, Brady S T and Gilbert S P 1982a Fast axonal transport in squid giant axon *Science* **218** 1127–9

Allen R D, Travis J L, Hayden J H, Allen N S, Breuer A C and Lewis L J 1982b Cytoplasmic transport: moving ultrastructural elements common to many cell types revealed by video-enhanced microscopy *Cold Spring Harb. Symp. Quant. Biol.* **46** 85–7

Andrews N L, Lidke K A, Pfeiffer J R, Burns A R, Wilson B S, Oliver J M and Lidke D S 2008 Actin restricts FcepsilonRI diffusion and facilitates antigen-induced receptor immobilization *Nature Cell Biol.* **10** 955–63

Bearer E L, Breakefield X O, Schuback D, Reese T S and LaVail J H 2000 Retrograde axonal transport of herpes simplex virus: evidence for a single mechanism and a role for tegument *Proc. Natl Acad. Sci. USA* **97** 8146–50

Bearer E L, DeGiorgis J A, Bodner R A, Kao A W and Reese T S 1993 Evidence for myosin motors on organelles in squid axoplasm *Proc. Natl Acad. Sci. USA* **90** 11252–6

Bearer E L and Reese T S 1999 Association of actin filaments with axonal microtubule tracts *J. Neurocytol.* **28** 85–98

Beeg J, Klumpp S, Dimova R, Gracia R S, Unger E and Lipowsky R 2008 Transport of beads by several kinesin motors *Biophys. J.* **94** 532–41

Brady S T, Lasek R J and Allen R D 1982 Fast axonal transport in extruded axoplasm from squid giant axon *Science* **218** 1129–31

Brady S T, Pfister K K and Bloom G S 1990 A monoclonal antibody against kinesin inhibits both anterograde and retrograde fast axonal transport in squid axoplasm *Proc. Natl Acad. Sci. USA* **87** 1061–5

Brown A, Wang L and Jung P 2005 Stochastic simulation of neurofilament transport in axons: the 'stop-and-go' hypothesis *Mol. Biol. Cell* **16** 4243–55

Cheng S B, Ferland P, Webster P and Bearer E L 2011 Herpes simplex virus dances with amyloid precursor protein while exiting the cell *PLoS One* **6** e17966

DeGiorgis J A, Reese T S and Bearer E L 2002 Association of a nonmuscle myosin II with axoplasmic organelles *Mol. Biol. Cell* **13** 1046–57

Fath K R and Lasek R J 1988 Two classes of actin microfilaments are associated with the inner cytoskeleton of axons *J. Cell Biol.* **107** 613–21

Galbraith J A, Reese T S, Schlief M L and Gallant P E 1999 Slow transport of unpolymerized tubulin and polymerized neurofilament in the squid giant axon *Proc. Natl Acad. Sci. USA* **96** 11589–94

Jaffe L A and Terasaki M 2004 Quantitative microinjection of oocytes, eggs, and embryos *Methods Cell Biol.* **74** 219–42

Jung P and Brown A 2009 Modeling the slowing of neurofilament transport along the mouse sciatic nerve *Phys. Biol.* **6** 046002

Kamal A, Almenar-Queralt A, LeBlanc J F, Roberts E A and Goldstein L S 2001 Kinesin-mediated axonal transport of a membrane compartment containing beta-secretase and presenilin-1 requires APP *Nature* **414** 643–8

Kamal A, Stokin G B, Yang Z, Xia C H and Goldstein L S 2000 Axonal transport of amyloid precursor protein is mediated by direct binding to the kinesin light chain subunit of kinesin-I *Neuron* **28** 449–59

Kanaan N M, Morfini G A, LaPointe N E, Pigino G F, Patterson K R, Song Y, Andreadis A, Fu Y, Brady S T and Binder L I 2011 Pathogenic forms of tau inhibit kinesin-dependent axonal transport through a mechanism involving activation of axonal phosphotransferases *J. Neurosci.* **31** 9858–68

Lazarov O *et al* 2005 Axonal transport, amyloid precursor protein, kinesin-1, and the processing apparatus: revisited *J. Neurosci.* **25** 2386–95

Li Y, Jung P and Brown A 2012 Axonal transport of neurofilaments: a single population of intermittently moving polymers *J. Neurosci.* **32** 746–58

Massey F J 1951 The Kolmogorov–Smirnov test for goodness of fit *J. Am. Stat. Assoc.* **46** 68–78

Morfini G, Szebenyi G, Elluru R, Ratner N and Brady S T 2002 Glycogen synthase kinase 3 phosphorylates kinesin light chains and negatively regulates kinesin-based motility *EMBO J.* **21** 281–93

Morfini G A *et al* 2009 Pathogenic huntingtin inhibits fast axonal transport by activating JNK3 and phosphorylating kinesin *Nature Neurosci.* **12** 864–71

Morris J R and Lasek R J 1984 Monomer–polymer equilibria in the axon: direct measurement of tubulin and actin as polymer and monomer in axoplasm *J. Cell Biol.* **98** 2064–76

Odell G M 1976 A new mathematical continuum theory of axoplasmic transport *J. Theor. Biol.* **60** 223–7

Pfister K K, Wagner M C, Stenoien D L, Brady S T and Bloom G S 1989 Monoclonal antibodies to kinesin heavy and light chains stain vesicle-like structures, but not microtubules, in cultured cells *J. Cell Biol.* **108** 1453–63

Reis G F, Yang G, Szpankowski L, Weaver C, Shah S B, Robinson J T, Hays T S, Danuser G and Goldstein L S 2012 Molecular motor function in axonal transport *in vivo* probed by genetic and computational analysis in Drosophila *Mol. Biol. Cell.* **23** 1700–14 PMID: 22398725

Sato-Yoshitake R, Yorifuji H, Inagaki M and Hirokawa N 1992 The phosphorylation of kinesin regulates its binding to synaptic vesicles *J. Biol. Chem.* **267** 23930–6 PMID: 1429730

Satpute-Krishnan P, DeGiorgis J A and Bearer E L 2003 Fast anterograde transport of herpes simplex virus: role for the amyloid precursor protein of Alzheimer's disease *Aging Cell* **2** 305–18

Satpute-Krishnan P, DeGiorgis J A, Conley M P, Jang M and Bearer E L 2006 A peptide zipcode sufficient for anterograde transport within amyloid precursor protein *Proc. Natl Acad. Sci. USA* **103** 16532–7

Schnapp B J and Reese T S 1989 Dynein is the motor for retrograde axonal transport of organelles *Proc. Natl Acad. Sci. USA* **86** 1548–52

Schnapp B J, Reese T S and Bechtold R 1992 Kinesin is bound with high affinity to squid axon organelles that move to the plus-end of microtubules *J. Cell Biol.* **119** 389–99

Schnapp B J, Vale R D, Sheetz M P and Reese T S 1985 Single microtubules from squid axoplasm support bidirectional movement of organelles *Cell* **40** 455–62

Schroer T A, Schnapp B J, Reese T S and Sheetz M P 1988 The role of kinesin and other soluble factors in organelle movement along microtubules *J. Cell Biol.* **107** 1785–92

Smith D A and Simmons R M 2001 Models of motor-assisted transport of intracellular particles *Biophys. J.* **80** 45–68

Solowska J M, Morfini G, Falnikar A, Himes B T, Brady S T, Huang D and Baas P W 2008 Quantitative and functional analyses of spastin in the nervous system: implications for hereditary spastic paraplegia *J. Neurosci.* **28** 2147–57

Szpankowski L, Encalada S E and Goldstein L S 2012 Subpixel colocalization reveals amyloid precursor protein-dependent kinesin-1 and dynein association with axonal vesicles *Proc. Natl. Acad. Sci. USA* **109** 8582–7

Terada S, Kinjo M, Aihara M, Takei Y and Hirokawa N 2010 Kinesin-1/Hsc70-dependent mechanism of slow axonal transport and its relation to fast axonal transport *EMBO J.* **29** 843–54

Terasaki M, Schmidek A, Galbraith J A, Gallant P E and Reese T S 1995 Transport of cytoskeletal elements in the squid giant axon *Proc. Natl. Acad. Sci. USA* **92** 11500–3

Vale R D, Reese T S and Sheetz M P 1985a Identification of a novel force-generating protein, kinesin, involved in microtubule-based motility *Cell* **42** 39–50

Vale R D, Schnapp B J, Reese T S and Sheetz M P 1985b Organelle, bead, and microtubule translocations promoted by soluble factors from the squid giant axon *Cell* **40** 559–69

Vermot J, Fraser S E and Liebling M 2008 Fast fluorescence microscopy for imaging the dynamics of embryonic development *HFSP J.* **2** 143–55